

Earth's albedo time series reveals low radiative energy input in December 2020

Antti Penttilä (✉ antti.i.penttila@helsinki.fi)

University of Helsinki <https://orcid.org/0000-0001-7403-1721>

Karri Muinonen

University of Helsinki <https://orcid.org/0000-0001-8058-2642>

Olli Ihalainen

VTT

Elizaveta Uvarova

University of Helsinki

Mikko Vuori

University of Helsinki

Guanglang Xu

University of Helsinki

Jyri Näränen

Finnish Geospatial Research Institute FGI

Olli Wilkman

FGI

Jouni Peltoniemi

Finnish Geospatial Research Institute FGI <https://orcid.org/0000-0002-4701-128X>

Maria Gritsevich

Finnish Geospatial Research Institute FGI

Heikki Järvinen

University of Helsinki

Alexander Marshak

NASA Goddard Space Flight Center

Article

Keywords: spherical albedo, Earth Polychromatic Imaging Camera, seasonal variation

Posted Date: July 16th, 2021

DOI: <https://doi.org/10.21203/rs.3.rs-677927/v1>

License: © ⓘ This work is licensed under a Creative Commons Attribution 4.0 International License.

[Read Full License](#)

1 Earth's albedo time series reveals low radiative energy input in December 2 2020

3 **A. Penttilä^{1*}, K. Muinonen^{1,2}, O. Ihalainen^{1,3}, E. Uvarova¹, M. Vuori¹, G. Xu^{1,5}, J. Näränen²,**
4 **O. Wilkman², J. Peltoniemi², M. Gritsevich^{2,6}, H. Järvinen⁴, A. Marshak⁷**

5
6 ¹Department of Physics, University of Helsinki, Finland

7 ²Finnish Geospatial Research Institute FGI, National Land Survey of Finland, Finland

8 ³VTT Technical Research Centre of Finland Ltd., Finland

9 ⁴Institute for Atmospheric and Earth System Research, University of Helsinki, Finland

10 ⁵Institute of Meteorology and Climate Research, Karlsruhe Institute of Technology, Germany

11 ⁶Institute of Physics and Technology, Ural Federal University, Ekaterinburg, Russia

12 ⁷NASA Goddard Space Flight Center, MD, USA

13 Abstract

14 The Earth's spherical albedo describes the ratio of light reflected from the Earth to that incident
15 from the Sun, an important input variable for the Earth's radiation balance. The spherical albedo has
16 been previously estimated from satellites in low-Earth orbits, and from light reflected from the
17 Moon. However, neither of these methods can produce continuous time series of the entire planet.
18 We developed a global method to derive the Earth's spherical albedo using the images from the
19 Earth Polychromatic Imaging Camera (EPIC) on board NOAA's Deep Space Climate Observatory
20 (DSCOVR). The satellite is located in the Lagrange 1 point between the Earth and the Sun and
21 observes the complete illuminated part of the Earth at once. The method allows us to provide
22 continuously updated spherical albedo time series data starting from 2015. This time series shows a
23 systematic seasonal variation with the mean annual albedo estimated as 0.295 ± 0.008 and an
24 exceptional albedo maximum in 2020, attributed to unusually abundant cloudiness over the
25 Southern Oceans.

26 Introduction

27 Solar radiation is the primary energy source of the Earth and largely determines Earth's climate.
28 The proportion of the incoming solar radiation reflected back to space by the Earth is described by
29 the spherical albedo. It depends on the reflective properties of the Earth and thus it is affected by the
30 proportion of the highly reflective areas relative to darker areas. For example, the melting of the
31 Antarctic and Greenland ice sheets results in increased absorption and decreased albedo. Hence, the
32 Earth's spherical albedo is a major factor behind the global weather and climate processes.
33 However, up to date there has not been a global, day-to-day estimate of the spherical albedo.

34 In the first half of the 20th century, estimates of the spherical albedo were based on an indirect
35 method of observing the Earth-lit Moon¹. These so-called earthshine observations depend on correct
36 estimations of the Moon's light-scattering properties, and thus they can be inaccurate and vary
37 considerably. The earliest satellite measurement of the spherical albedo was made in 1959 by the
38 Explorer 7 satellite and its value has remained approximately 0.3 ever since². Since 1997 the albedo
39 is being overseen by the Clouds and the Earth's Radiant Energy System (CERES), which includes

40 five satellites and seven CERES instruments³. As of 2017, only five instruments are operational. As
41 it takes numerous hours for the CERES to scan the entire Earth while the cloud cover of the Earth
42 evolves in a matter of minutes, the spherical albedo evaluation method by the CERES instruments
43 produces noticeable uncertainties in the measured albedo value^{2,3}.

44 To measure the spherical albedo directly one needs to simultaneously detect radiation reflected by
45 the Earth from all directions, which renders such measurements impossible. To circumvent this, we
46 use the Earth Polychromatic Imaging Camera (EPIC) on board the Deep Space Climate
47 Observatory (DSCOVR) spacecraft combined with angular distribution models provided by the
48 CERES based on many years of dedicated measurements. The DSCOVR is a spacecraft orbiting in
49 the Lagrange point 1 around 1.5 million kilometers from the Earth, which allows the EPIC to
50 always view practically the entire sunlit hemisphere of the Earth. The DSCOVR was launched in
51 2015, and the EPIC has been operational ever since apart from one six-month maintenance break in
52 2019⁴.

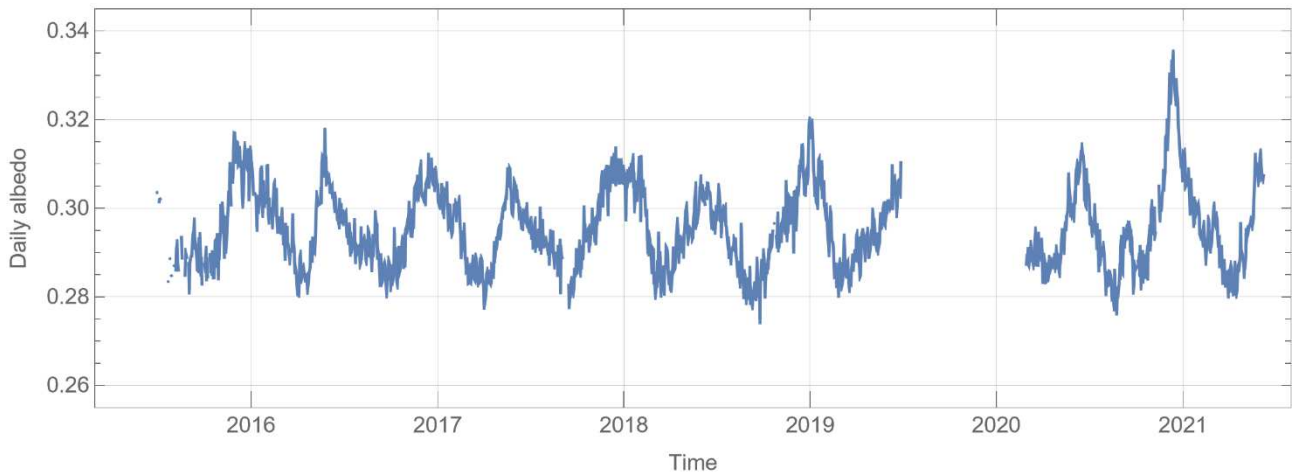
53 Data from the instruments allows us to propose an algorithm that automatically translates
54 directional reflectance obtained from the EPIC images into estimated value of short-wave spherical
55 albedo. We have launched a web service that collects the computed spherical albedo of the Earth
56 from the whole operational period and updates the data daily with the latest observations⁵. This is
57 the first global daily time series of the Earth's albedo and it spans already now over seven years in
58 time. This enables us to analyze the pattern of temporal variation in albedo over a year which
59 demonstrates anomalies in albedo behavior. The accurate estimate of the short-wave spherical
60 albedo is important in evaluating the energy balance of the Earth system.

61 Results

62 The EPIC images constitute a time series of the sunlit part of the Earth, including atmosphere,
63 starting from June 2015 and still running. There are usually about 22 images per day during
64 Northern Hemisphere summer, and 13 during winter. Each multispectral image has 10 wavelength
65 channels between 317 and 780 nm. The channels have full-width-at-half-maximum values between
66 1 and 3 nm⁶⁻⁹.

67 Each image pixel represents the radiance reflected by the corresponding surface area on the Earth.
68 This radiance is a function of the reflective properties of the surface, and the solar and satellite
69 angles. The DSCOVR satellite is located in the first Lagrange point between the Earth and the Sun,
70 therefore the radiance is observed close to backscattering geometry with satellite and solar angles
71 being almost equal. To convert measured radiances at backscattering into integrated albedo values
72 at top-of-atmosphere (ToA), we apply the angular distribution models (ADMs) provided by the
73 CERES project^{10,11}. The ADMs are provided for several surface types and cloud fractions, and we
74 combine these into four types for our analysis: clear and cloudy land and ocean. The reason for this
75 is that the angular resolution of the tabulated ADMs is only 10 degrees, and we want to interpolate
76 with a finer resolution in the backscattering direction and combining similar surface types gives us
77 more robust estimation (see Methods). Additionally, estimating temporary cloud fractions from
78 EPIC images is challenging, a more robust method can be developed for simple clear versus cloud-
79 covered surface estimation. Land or ocean surface classification is available from the International
80 Geosphere–Biosphere Programme, and temporal cloud coverage we estimate from the EPIC images
81 using logistic regression model with input from EPIC channels at 325, 551, and 780 nm.

82 The ToA albedo values for each pixel over the Earth’s sunlit disk are averaged for albedo of the
83 Earth at each wavelength channel. Finally, the per-wavelength albedos are summed with weights
84 from incident solar spectra at each channel, obtained from National Oceanic and Atmospheric
85 Administration (NOAA) climate data record of solar spectral irradiance¹². The solar spectrum is
86 taken as constant in this study with only the distance between the Earth and the Sun influencing the
87 total flux level. The channels at 688 and 764 nm in EPIC images are left out since they are targeted
88 to measure atmospheric O₂ at narrow absorption bands. The resulting time series of Earth’s daily
89 albedo is shown in Figure 1.



90

91 Figure 1: Daily average of Earth’s albedo over the whole operational time of the EPIC camera.

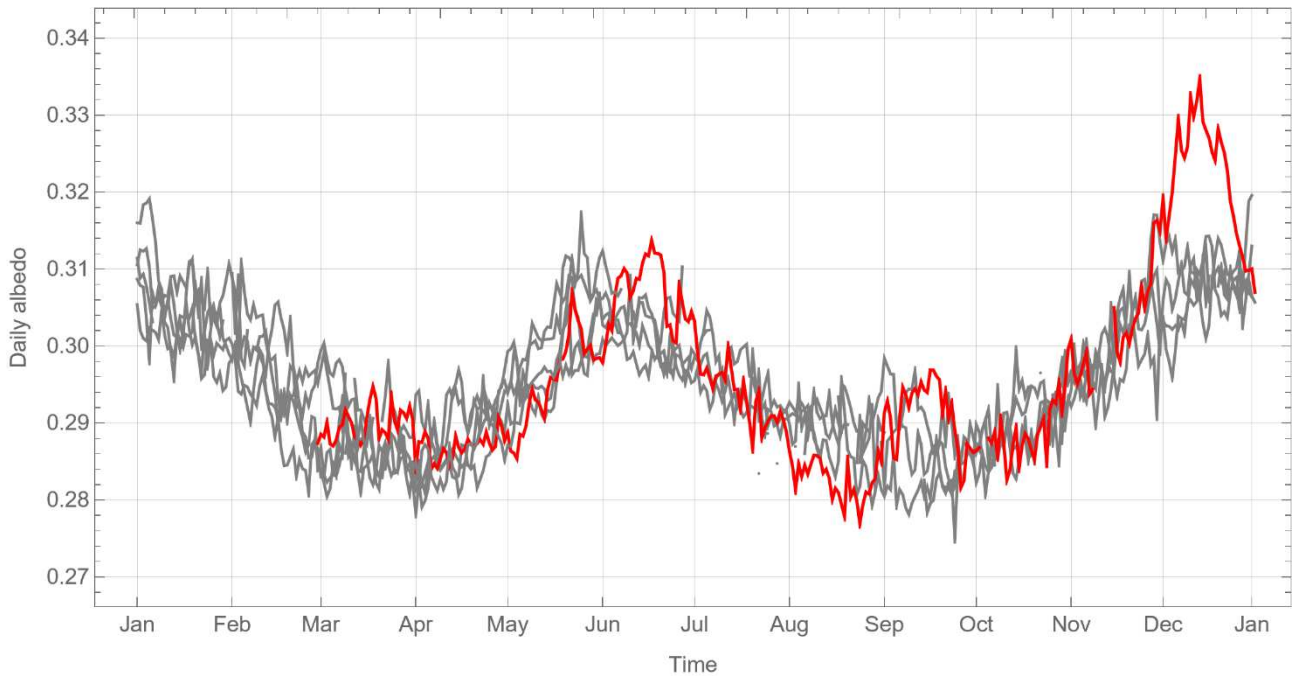
92

93 The daily averaged time series has been filtered to remove outliers. For some EPIC images, not all
94 the wavelength channels are present. If there is not a proper coverage of usable images over the day,
95 some parts of the Earth are not present, and this would introduce a bias to the mean albedo of that
96 day. Therefore, these days are left out from our time series data. There is a period between late 2019
97 and early 2020 when the EPIC camera was not operational.

98 We can derive the mean yearly spherical albedo of the Earth, at visual wavelengths, by grouping the
99 daily time series values by the day in the year, averaging per day, and finally averaging over days in
100 a year. From the currently available data, this value is $29.5 \pm 0.8 \%$. The value agrees well with
101 earlier estimates of 28.6–30.1 % by satellites in low-Earth orbits, see Kandel and Viollier (2010)²,
and 29.7 % from earthshine measurements done by observing the Moon, see Goode et al. (2001)¹⁴.

102 There is an evident annual cycle of the albedo. This can be seen more clearly from Figure 2 where
103 the years have been stacked together. The year 2020 is highlighted with a red color because of the
104 anomaly in the second annual maximum usually present between December and January. In the
105 EPIC data, there are observations of four other Northern Hemisphere winter maxima, but the one in
106 2020–21 is significantly higher.

107



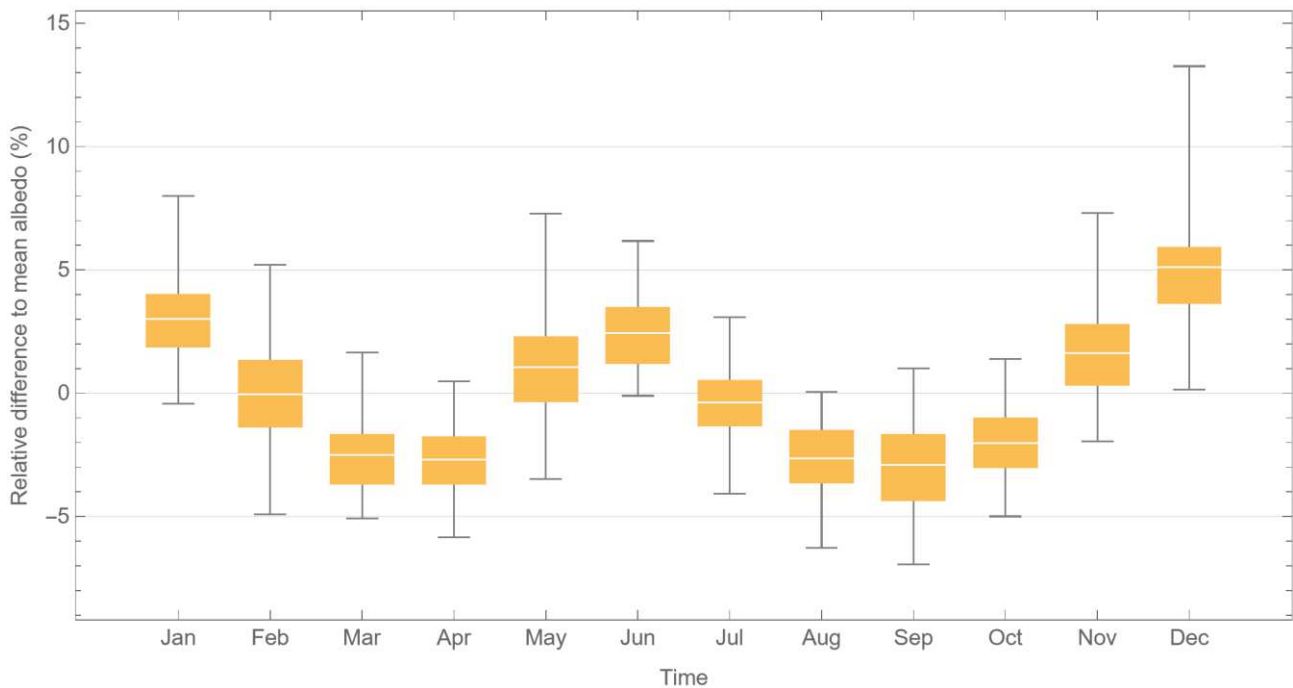
108

109 Figure 2: Daily averages of Earth's albedo with all years stacked together. Data from the year 2020 is highlighted with
 110 red color, years 2015–2019 and 2021 are shown in gray.

111 We can verify the anomaly in December 2020 statistically by studying the monthly averages for
 112 each year. The combined monthly averages are shown in Figure 3, plotted as variations from the
 113 overall average albedo in a box-and-whiskers chart. The one-way analysis-of-variance test of the
 114 differences in the mean values over several sets of observations (different years over a month) can
 115 find significant (p -value less than 0.1 %) differences for all months. However, by far the smallest p -
 116 value, and therefore the largest difference, is for December, formally less than 10^{-29} .

117 When conducting t -tests for year pairs inside a month, we find that the only year which differs from
 118 all the other years when using the Bonferroni-corrected p -value limit of $0.001/m_i$, where m_i is the
 119 number of year data sets on month i , is the year 2020 and months August and December. From
 120 these analyses we conclude that the largest yearly variations in a month are on December, and that
 121 is mainly due to year 2020.

122



123

124 Figure 3: Monthly variation in the daily averages of Earth's spherical albedo. Values are relative differences from the
 125 overall mean albedo of 0.295. The horizontal white line shows the average over the month, the box indicates the range
 126 from 1st quarter to 3rd quarter, and the lines the range from minimum to maximum.

127 We can conclude on the results on temporal variation on Earth's spherical albedo by summarizing
 128 that there are two maxima and two minima. The main maximum occurs in December–January
 129 during the Southern Hemisphere summer, and the secondary maximum in June during the Northern
 130 Hemisphere summer. The minimum values are on March–April, and on September. The coefficient
 131 of variation, that is the standard deviation divided by mean, of the daily average values over a year
 132 is 2.7 %, and the range of minimum-to-maximum deviation of the daily averages from annual
 133 average is 0.031 (10.3 percentage points in scale relative to the mean annual albedo). In December
 134 2020, the daily albedo values were up to 0.023 (7.2 %, on Dec 13) larger than the average daily
 135 value over all the years.

136 Discussion

137 The annual variation of the Earth's spherical (Bond) albedo is described for the first time in detail.
 138 Previous investigations mainly describe the variations on the incident solar flux due to the Earth's
 139 elliptic orbit (see Fig. 5 in Kandel and Viollier 2010²), as for us, this effect is considered and
 140 properly accounted for. The accurate annual albedo behavior enables the detailed analysis of local
 141 geographic and atmospheric effects on the albedo during a year.

142 The Earth contains regions of low albedo (e.g., cloud-free ocean areas, vegetated land areas) and
 143 high albedo (e.g., clouds, ice and snow surfaces, sandy deserts). Diurnal and annual variations in the
 144 albedo time series (Figure 1, Figure 3) result from a modulation of these two aspects, depending on
 145 the apparent longitude (diurnal variations) and latitude (annual variations). Especially, the cloud-
 146 covered ocean areas increase the albedo. The daily cloud-covered ocean fraction, estimated from
 147 the EPIC images, has the correlation coefficient value of 86 % with the daily albedo value (see
 148 Figure 6).

149 In annual albedo variations, the main albedo maximum occurs in December when the Antarctic ice
150 sheet, sea ice, and snow cover are visible entirely. At this time, cloud formations of the mid-latitude
151 cyclones over the Southern Ocean are well pronounced. Albedo is further enhanced by the shallow
152 convective cloud cover over the subtropical oceans and the relatively small areas of cloud-free
153 ocean areas visible, on average, at this time of the year.

154 The secondary albedo maximum occurs in June when the Greenland ice sheet and sea ice in the
155 Arctic Ocean are well exposed. Cloud formations of the mid-latitude cyclones of the North Atlantic
156 and Pacific storm tracks are active, although reduced from their winter maxima. Subtropical desert
157 areas are mostly cloud free exposing also these high surface albedo areas. Deep convective clouds
158 of the inter-tropical convergence zone are on the Northern Hemisphere at this time of the year.
159 Again, relatively little cloud-free ocean areas are visible.

160 The main albedo minimum precedes the main maximum in August–September when neither of the
161 Polar regions is visible. At this time of year, there are relatively few shallow convective clouds over
162 the subtropical Northern Atlantic and Pacific, as well as over the Mediterranean. North Atlantic and
163 Pacific storm track activities are near to their minima. Also, vegetation is at its maximum extent in
164 the Sahel region. Monsoon is in active phase over the Indian peninsula and South-East Asia, thus
165 enhancing the albedo. The secondary minimum precedes the secondary maximum in March–April.

166 The solar energy input at the Earth's average distance from the Sun is 1361 W/m^2 for the sunlit
167 disk of the Earth over all wavelengths, and the EPIC filters range from 317 nm to 780 nm in
168 wavelength¹². The portion of the solar input between these wavelengths is 52.7%. In ultraviolet
169 below 317 nm there is only 0.5% of the total energy. We assume that the albedo derived here for
170 the range 317–780 nm is valid for somewhat longer wavelengths and estimate roughly that our
171 shortwave albedo is valid for at least 60% of the reflection or absorption of the total solar input.
172 With this estimate, the input energy that is absorbed into the area of sunlit Earth's disk and
173 atmosphere is about 4.9 W/m^2 more during the albedo minimum in September than on average.
174 During the albedo maximum in December, about 8.7 W/m^2 less energy is absorbed.

175 An exceptional albedo occurred on 13 December 2020 and persisted for about a week before and
176 after the peak value. This anomaly coincides with the main annual maximum in December. Our
177 main explanation is a short-lived and exceptional maximum in the amount of shallow convective
178 clouds over the subtropical Indian Ocean and the Pacific east of Australia, see Figure 4. The
179 development of exceptionally wide shallow cloud cover coincides and is favoured by a constellation
180 of several mature mid-latitude cyclones, feeding moist air from the subtropics towards the
181 Antarctic. At the time of the maximum albedo, all relevant large-scale atmosphere-ocean indicators
182 were in close-to-neutral stages: the Madden-Julian oscillation (MJO) phase centre was in the
183 Oceanic continent, but the amplitude was weak; the Indian Ocean Dipole (IOD) was neutral; El
184 Niño – Southern Oscillation (ENSO) was in a weak La Niña phase (El Niño 3.4 index) and
185 returning to neutral.

186



188 Figure 4: EPIC natural color constructed images, taken at 2020-12-13 at 04:40 UCT (left), and 2020-08-04 at 22:25
 189 UCT (right). The image on the left has one of the largest albedos in 2020 (0.350), and the image on the right has one
 190 of the lowest (0.253). Image credits: NASA EPIC team, <https://epic.gsfc.nasa.gov/>.

191

192 In December 2020, the EPIC-derived daily albedo was elevated to 0.334 from its typical December
 193 value of 0.312 in 2015–19. Assuming these to represent well the planetary reflectivity, the emission
 194 temperature of the Earth would decrease by 2.1 K through a 7.8 W/m^2 reduction in the absorbed
 195 solar radiation. For comparison, the global mean sensible heat flux from the Earth surface to the
 196 atmosphere amounts to about 20 W/m^2 and the absorbed solar radiation in the atmosphere to about
 197 80 W/m^2 ¹⁴. It is therefore fair to treat the short-term albedo peak in December 2020 as quite
 198 remarkable.

199 Methods

200 Cloud classification in EPIC images

201 The algorithm for cloud classification in the EPIC images was trained with a manually prepared
 202 data set of spectral radiances together with subjective cloudy/clear label decision. For image data,
 203 we collected images from the first week of every month in 2018. We converted the original HDF5
 204 library data for one multi-channel image into PNG image stack of all the wavelength channels. We
 205 opened the image stacks in ImageJ¹⁵, and manually selected areas of either clear or cloud-covered
 206 land and ocean surfaces. The spectral radiance values of pixels within these areas were recorded
 207 together with the label (1) clear land / (2) clear ocean / (3) cloud-covered surface. Altogether, we
 208 produced 338 areas of clear land, 331 areas of clear ocean, and 481 areas of cloud-covered surfaces.
 209 Each area contains several tens of pixels, the mean values over the areas were employed in the
 210 analysis. The ice sheet covered areas, such as Antarctica, are indistinguishable from cloud-covered
 211 surfaces.

212 A logistic regression model was separately fitted into data with clear land and cloud-covered
213 surfaces, and data with clear ocean and cloud-covered surfaces. A logistic regression model has a
214 linear function modeling the log-odds of the probability of an event. In our case, the event is that the
215 surface is covered with clouds. With some algebra the model can be written as

$$216 \quad p = \frac{1}{1 + e^{-(\beta_0 + \beta_1 x_1 + \dots + \beta_k x_k)}}$$

217 where p is the probability of cloud-cover, and $\beta_0 + \beta_1 x_1 + \dots + \beta_k x_k$ is the linear function with
218 unknown coefficients β_i and known radiances x_i from channels $1, \dots, k$.

219 We executed forward-selection stepwise regression to optimize the model with the best value of the
220 Bayesian Information Criterion (BIC) statistics of the model. We ended up with models with a
221 constant coefficient β_0 and three coefficients for the EPIC wavelength channels at 325, 551, and
222 780 nm. For land vs. clouds model, all the four coefficients were tested significant with p -values
223 less than 0.1 %. For ocean vs. clouds model, all other but the coefficient for the channel 780 nm
224 were significant with the same p -value limit.

225 Scattering geometry and interpolation of angular distribution models

226 We found it realistic to successfully classify pixels of clear or cloudy land or ocean surface from the
227 EPIC images, but not different cloud types (water or ice) or levels of cloud cover that are present in
228 CERES angular distribution models (ADMs). ADMs are also divided into different wind speeds for
229 ocean and into different vegetation types for land. To exploit these, wind speeds on ocean pixels
230 would need to be connected from weather models into our analysis together with up-to-date land
231 cover information. This is a bit cumbersome but could be done. However, we decided to emphasize
232 more the interpolation of the scattering geometry inside the ADM models over having many
233 ocean/surface/cloud subtype ADMs.

234 The scattering geometry in the EPIC observations is such that the observation is always done close
235 to backscattering. The phase angle between the Sun and the DSCOVR spacecraft, as seen from the
236 Earth, is below 12° except for few rare cases in years 2020–21. On average, phase angle has been
237 8.2° . After the break in the DSCOVR operations in 2019, the minimum phase angle has gradually
238 started to decrease (see Figure 6). It was never below 4° before 2020, but now the minimum value
239 is 1.8° .

240 While in terms of phase angle EPIC is observing close to backscattering, the local Sun zenith angle
241 on each Earth pixel varies between 0° and 90° . The ADM tables, on the other hand, have 10° bins
242 for all the three angles (Sun zenith, observer zenith, azimuth). So, our backscattering geometry
243 implies that we need ADM table values inside cells where Sun and observer zenith angles are in the
244 same bin and azimuth angle is in the bin 0 – 10° . Thus, the 3-dimensional (in angle) ADM tables will
245 reduce for our purposes to 1-dimensional tables that can be parametrized with Sun zenith angle
246 only.

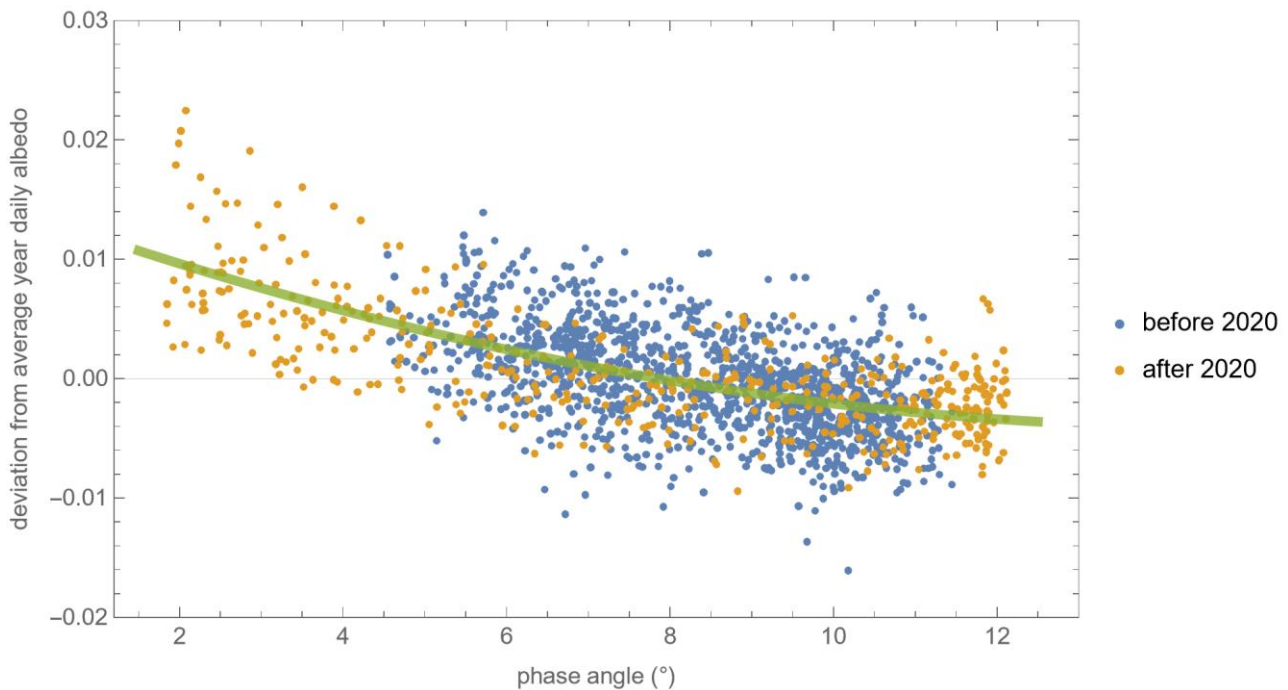
247 We find the reduced 1-d table binning of 10° too coarse as it would introduce inaccuracies when
248 applied to pixels having Sun zenith angle anywhere between 0° and 90° . Therefore, we interpolate
249 the reduced ADM tables over 0° and 90° range and use these interpolated coefficients when
250 converting ToA radiances measured by EPIC into integrated ToA albedos. We find that the reduced
251 1-d tables show relatively similar behavior for all clear ocean surfaces regardless of the wind speed,
252 for all clear land surfaces, and for all cloud-covered surfaces regardless of the cloud type or

253 coverage. Thus, our final set of ADM coefficients come from interpolated data on these three
254 categories, averaged over their subtypes.

255 Effect of phase angle on albedo

256 The phase angle of EPIC observations varies between 2° and 12° . After DSCOVR operations break
257 in 2019 the phase angle variation has increases and the minimum phase angle has decreased from
258 previous 4° to 1.8° . These decreasing phase angles introduce possible source of bias in our albedo
259 estimation. The resolution in the binned data of the ADM models is 10° in all three angles,
260 indicating that we do not have exact information on how possible backscattering effects (self-
261 shadowing, coherent backscattering) are behaving on small phase angles inside this bin.

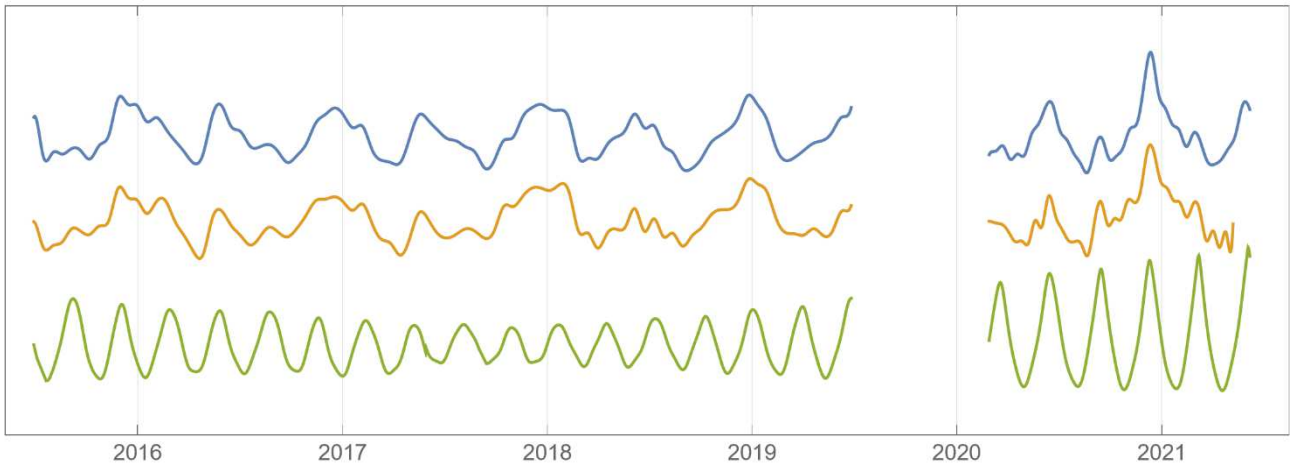
262 Currently, we can only estimate the possible bias resulting from small phase angles. We can do this
263 by computing the deviations of daily albedo values from the average-year albedo values, and by
264 modeling how they are changing as a function of the observation phase angle. From Figure 5 we
265 can see that there is obvious correlation between these. Decreasing phase angles are introducing a
266 positive bias, on average, into the albedo values. A second-degree linear fit has the p -values of all
267 the model coefficients significant below 0.1 % level, and a slightly better value (0.37) of adjusted
268 R^2 measure of the model than with first-degree model (0.36). According to this model, there can be
269 up to 0.01 positive average bias coming from the phase angle effect if phase angle approaches 2° .



270

271 Figure 5: Differences between daily albedo values and corresponding values from average year, as a function of the
272 phase angle of the observation. The solid line shows the 2nd degree linear fit to data. The data before and after the
273 DSCOVR operations break in 2019–2020 is shown with different colors, but the model is fit on both sets together.

274 This same bias can also be roughly estimated from the small upturns in daily albedo values in
275 November 2020 and March 2021, see Figure 1 and Figure 6. These upturns are simultaneous with
276 local phase angle minima of about 2° . Graphical estimation of possible excess in albedo values in
277 these upturns also suggests a value of 0.01 at most.



278

279
280
281

Figure 6: Daily average albedo values (blue lines), daily average fraction of clouds over oceans (orange lines), and scattering angle of EPIC observations (green lines). The scattering angle is the complement of the phase angle α , that is, $180^\circ - \alpha$. The curves have been shifted in vertical direction and rescaled for improved visualization.

282
283
284
285
286

The exceptional albedo values in December 2020 were at most 0.023 larger than the average December value. This exceptional value was received at the time of local phase angle minima of the DSCOVR spacecraft, 2.1° . We conclude that the effect of the phase angle can explain, at maximum, about half of the difference, and that December 2020 is exceptional in our albedo time series even if taking the possible phase angle effect into account.

287

References

288
289
290
291
292
293
294
295
296
297
298
299
300
301
302
303
304
305
306
307

- 1 Stephens GL, O'Brien D, Webster PJ, Pilewski P, Kato S, and Li J (2015). The albedo of Earth. *Reviews of Geophysics* 53(1), 141–163. DOI: 10.1002/2014RG000449.
- 2 Kandel R and Viollier M (2010). Observation of the Earth's radiation budget from space. *Comptes Rendus Geoscience*, 342(4), 286–300. DOI: j.crte.2010.01.005.
- 3 Wielicki BA, Barkstrom BR, Harrison EF, Lee RB, Smith GL, and Cooper JE (1996). Clouds and the Earth's Radiant Energy System (CERES): An Earth Observing System Experiment. *Bulletin of the American Meteorological Society* 77(5), 853–868. DOI: 10.1175/1520-0477(1996)077<0853:CATERE>2.0.CO;2.
- 4 Marshak A, Herman J, Adam S, et al. (2018). Earth observations from DSCOVR EPIC instrument. *Bulletin of the American Meteorological Society* 99(9), 1829–1850. DOI: 10.1175/BAMS-D-17-0223.1.
- 5 Earth Spherical Albedo — From DSCOVR/EPIC Satellite Images. Web page, <http://albedo.physics.helsinki.fi/>.
- 6 Herman JR, Huang L, McPeters RD, Ziemke J, Cede A, and Blank K (2018). Synoptic ozone, cloud reflectivity, and erythemal irradiance from sunrise to sunset for the whole Earth as viewed by DSCOVR spacecraft from the earth-sun Lagrange-1. *Atmospheric Measurement Techniques* 11, 1–18.
- 7 Geogdzhayev I, and Marshak A (2018). Calibration of the DSCOVR EPIC visible and NIR channels using MODIS Terra and Aqua data and EPIC lunar observations. *Atmospheric Measurement Techniques* 11, 359–368. DOI: 10.5194/amt-11-359-2018.

- 308 8 Ohtake M, Matsunaga T, Yokota Y, Yamamoto S, Ogawa Y, Morota T, Honda C, Haruyama J,
309 Kitazato K, Takeda H, Iwasaki A, Nakamura R, Hiroi T, Kodama S, and Otake H (2010).
310 Deriving the absolute reflectance of lunar surface using SELENE (Kaguya) Multiband Imager
311 data. *Space Science Reviews* 154, 57–77.
- 312 9 Ohtake M, Pieters CM, Isaacson P, Besse S, Yokota Y, Matsunaga T, Boardman J, Yamamoto
313 S, Haruyama J, Staid M, Mall U, and Green RO (2013). One Moon, many measurements 3:
314 Spectral reflectance. *Icarus* 226, 364–374.
- 315 10 Su W, Corbett J, Eitzen Z, and Liang L (2015). Next-generation angular distribution models for
316 top-of-atmosphere radiative flux calculation from CERES instruments: methodology. *Atmospheric
317 Measurement Techniques* 8, 611–632. DOI: 10.5194/amt-8-611-2015.
- 318 11 Su W, Corbett J, Eitzen Z, and Liang L (2015). Next-generation angular distribution models for
319 top-of-atmosphere radiative flux calculation from CERES instruments: validation. *Atmospheric
320 Measurement Techniques* 8, 3297–3313. DOI: 10.5194/amt-8-3297-2015.
- 321 12 Coddington O, Lean JL, Lindholm D, Pilewskie P, Snow M, and NOAA CDR Program (2015).
322 NOAA Climate Data Record (CDR) of Solar Spectral Irradiance (SSI), NRLSSI Version 2.
323 NOAA National Centers for Environmental Information. DOI:10.7289/V51J97P6, accessed
324 2020-10-21.
- 325 13 Goode PR, Qiu J, Yurchyshyn V, Hickey J, Chu M-C, Kolbe E, Brown CT, and Koonin SE
326 (2001). Earthshine observations of the Earth's reflectance. *Geophysical Research Letters*, 28(9),
327 1671–1674. DOI: 10.1029/2000GL012580.
- 328 14 Hartmann D (2015). *Global Physical Climatology*. Elsevier Science. 2nd Edition, ISBN:
329 9780123285317, 498 pp.
- 330 15 ImageJ software. URL <https://imagej.github.io/>.

331 Acknowledgements

332 We gratefully acknowledge funding received from the Academy of Finland (grant numbers 298137
333 and 1333034). Computational resources are provided by CSC — IT Center for Science Ltd.,
334 Finland.

335 Author contributions

336 The method and algorithm were designed by A.P., K.M. O.I., E.U., M.V., G.X., and O.W.. The
337 algorithm was coded by A.P., O.I., E.U., M.V., and O.W.. The web service was designed by A.P.,
338 K.M., E.U., M.V., and coded by A.P. and M.V.. The data in this article was prepared by A.P., as
339 well as the statistical analysis on the data. The article was written by A.P., K.M., E.U., M.G., and
340 H.J.. All authors provided input and comments to the article.

341 Competing interests

342 No

343 **Materials & Correspondence**

344 Antti Penttilä, antti.i.penttila@helsinki.fi